

Rapid Rotation of Polarization Orientations in PSR B1919+21's Single Pulses:  
Implications On Pulsar's Magnetospheric Dynamics

SHUNSHUN CAO,<sup>1</sup> JINCHEN JIANG,<sup>2</sup> JAROSLAW DYKS,<sup>3</sup> KEJIA LEE,<sup>1,4,2</sup> JIGUANG LU,<sup>2,5</sup> LUCY S. OSWALD,<sup>6</sup>  
WEIYANG WANG,<sup>7</sup> AND RENXIN XU<sup>1,4</sup>

<sup>1</sup>*Department of Astronomy, School of Physics, Peking University, Beijing 100871, China*

<sup>2</sup>*National Astronomical Observatories, Chinese Academy of Sciences, Beijing 100012, China*

<sup>3</sup>*Nicolaus Copernicus Astronomical Center, Polish Academy of Sciences, Rbianańska 8, 87-100, Toruń, Poland*

<sup>4</sup>*Kaoli Institute for Astronomy and Astrophysics, Peking University, Beijing 100871, China*

<sup>5</sup>*Guizhou Radio Astronomical Observatory, Guiyang 550025, China*

<sup>6</sup>*School of Physics and Astronomy, University of Southampton, Southampton SO17 1BJ, UK*

<sup>7</sup>*School of Astronomy and Space Science, University of Chinese Academy of Sciences, Beijing 100049, China*

(Received; Revised; Accepted)

Submitted to ApJL

ABSTRACT

We analyse and model rapid rotations of polarization orientations in PSR B1919+21's single pulses, based on FAST observation data. In more than one third of B1919+21's single pulses, polarization angle (PA) is found to rotate quasi-monotonically with pulse longitude, by over 180 or even 360 degrees. Most of these quasi-monotonic PA curves have negative slopes with respect to pulse longitude. Oscillations of circular polarization fraction accompany these PA rotations. This rapid rotation could be induced by quick change of phase lag between normal wave modes within an individual pulse. We propose a phenomenological model to successfully reproduce the observed polarization rotations in single pulses, and calculate phase lags in a dipolar magnetic field of an aligned rotating pulsar, with a dispersion relation of orthogonal wave modes in strongly magnetized plasma. The weak frequency dependence of observed polarization rotation requires the radio emission height to be low, approximately 10 times the neutron star radius.

*Keywords:* polarimetry — radio pulsars: individual: B1919+21 — neutron stars — radiative processes — magnetospheric radio emissions — plasma astrophysics

1. INTRODUCTION

The highly magnetized relativistic plasma spheres around neutron stars, i.e. magnetospheres, generate and modify pulsars' radio emission (see [Philippov & Kramer 2022](#) for a review). Magnetospheres not only play a vital role in pulsar and neutron star theories, but are also natural laboratories for particle experiments (e.g., [Noordhuis et al. 2023](#); [Xue et al. 2023](#)).

Among theoretical, especially analytical studies, much effort has been focused on analyzing normal wave modes in magnetospheres. A fundamental property of the magnetosphere is the birefringence, so dispersion relations of the ordinary (O) mode and the extraordinary (E/X) mode are the basis for further analysis of wave propagation. [Melrose & Stoneham \(1977\)](#) derived the dispersion relations of O and E modes in a cold relativistic plasma with a single bulk velocity value and infinitely large magnetic field strength, and naturally explained pulsars' orthogonal polarization modes observed by [Manchester et al. \(1975\)](#). Such dispersion relations have been applied to describe ray trajectories in pulsar magnetospheres (e.g., [Barnard & Arons 1986](#); [Petrova & Lyubarskii 2000](#)) and to explain the origin of circular

polarization in pulsar radio emissions (e.g., Lyubarskii & Petrova 1998), involving calculating the phase lag between wave modes.

Despite the success of models, some parameters in pulsar magnetospheres are not well-constrained. Two key parameters are the plasma multiplicity  $\kappa$ , defined as the ratio between the actual plasma density and the Goldreich-Julian particle number density (equation (9) in Goldreich & Julian 1969), and the Lorentz factor of the “secondary” plasma particles,  $\gamma_{\text{sec}}$ . The “secondary” plasma particles are electron positron pairs produced in polar cap pair cascade processes. The Lorentz factor of these particles is also related to the emission height, the distance between emission point and pulsar centroid. Usually  $\kappa$  takes the value  $10^3 \sim 10^5$ , and  $\gamma_{\text{sec}}$  takes the value  $10 \sim 10^3$  (e.g., Philippov & Kramer 2022). Beside some attempts to achieve more realistic simulations, studying observations’ connection with theories is important for pushing studies forward. The double pulsar system J0737–3039 has provided good observational constraints on the magnetospheric physics (Lyutikov & Thompson 2005; Lower et al. 2024). However, for solitary pulsars, detailed studies of individual pulse behaviours might bring us more insight into pulsar magnetospheres, with China’s the Five-hundred-meter Aperture Spherical radio Telescope (FAST) now providing a large amount of high-quality radio pulsar data.

In this letter we present our analysis and modeling of some rapid polarization position angle (PA) rotations in PSR B1919+21’s single pulses, based on FAST data. As the first pulsar ever discovered (Hewish et al. 1968), B1919+21 is frequently studied under various frequency bands. It is a typical normal pulsar with  $P = 1.34$  s and  $\dot{P} = 1.35 \times 10^{-15}$  (Manchester et al. 2005). B1919+21 exhibits sub-pulse drifting, with drifting properties changing with frequency (Cordes 1975; Proszynski & Wolszczan 1986). It was also found to exhibit unusual radius-frequency-mapping (RFM), with its pulse profile width slightly getting wider when frequency increases (Mitra & Rankin 2002; Hassall et al. 2012; Pilia et al. 2016). Besides, polarization studies on this pulsar have shown that the single pulses’ PA distribution changes significantly with frequency (Mitra et al. 2015; Olszanski et al. 2019). Dyks (2017, 2019) modelled the 45 degree PA jumps observed in B1919+21 (Mitra et al. 2015) through the coherent superposition of orthogonally polarized proper mode waves. Primak et al. (2022) have identified a slow rotation of polarization direction within a limited longitude range. The rotations occurred on the time scale of subpulse drift and led to a torus-shaped distribution of polarization states in Stokes space. Our work will further investigate single pulses’ polarization patterns, and try to relate them to theoretical issues in pulsar magnetospheres.

In Section 2, basic information on observation and data reduction is given. Section 3 shows the observed results ranging from basic properties of the integrated profile and the highly linearly polarized profile, to single pulses’ distribution patterns, and finally the rapid rotating polarization orientations in individual single pulses. In Section 4 we develop the model to explain the quick rotating single pulse polarization orientations in two steps: firstly a phenomenological model for reproducing the observed polarization patterns and exploring the parameter space, secondly the normal modes’ phase lag calculation in a more realistic magnetosphere, with known dispersion relation. We propose that the key factor to understand the polarization pattern is the phase lag value between orthogonal modes. Discussions on model feasibility, B1919+21’s precursor component, asymmetries in B1919+21’s polarization pattern and possible particularity of B1919+21 are presented in Section 5. Section 6 summarizes the conclusions.

## 2. OBSERVATION AND DATA REDUCTION

Two epochs of observation on 2023 August 23 and 2023 September 30, are used in this paper. All of them were made by FAST at small zenith angles ( $< 26.4^\circ$ ), with the L-band 19-beam receiver (Jiang et al. 2020). The data were recorded under the frequency band 1000 MHz to 1500 MHz, and the band was divided into 4096 channels. The time resolution of the recording is  $49.152\mu\text{s}$ . At the beginning of each observation, modulated signals from a noise diode were injected as a 100% linearly polarized source for polarimetric calibration. The data processing (including folding, RFI mitigation, calibration, and timing) is done with software packages DSPSR (van Straten & Bailes 2011), PSRCHIVE (Hotan et al. 2004) and TEMPO2 (Hobbs et al. 2006). We get 2947 pulses in total, and each pulse period is divided into 4096 bins. In this paper, we follow the PSR/IEEE convention for the definition of Stokes parameters (van Straten et al. 2010). To correct the bias in calculating linear polarization intensity  $L$  through  $L = \sqrt{Q^2 + U^2}$ , we remove  $L$ ’s baseline in every pulse by subtracting averaged  $L$  values in off-pulse longitude ranges.

## 3. RESULTS

### 3.1. Overview of integrated profiles’ properties

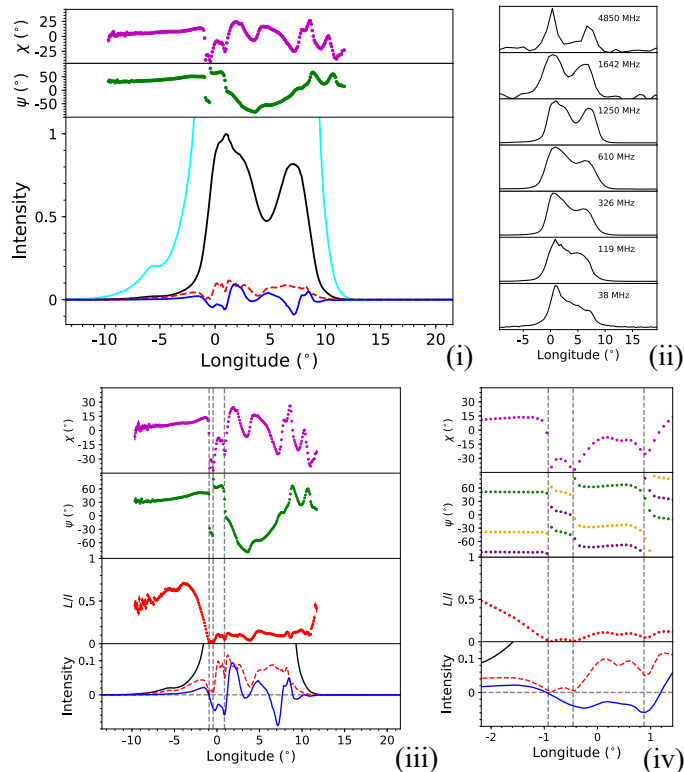


**Figure 1.** (i) Integrated profile of 2947 pulses of B1919+21. Black line - total intensity ( $I$ ); Cyan line - 10 times total intensity ( $10 \times I$ ); red dashed line - linear polarization intensity ( $L = \sqrt{Q^2 + U^2}$ ); blue line - circular polarization intensity ( $V$ ).  $I$ ,  $L$  and  $V$  are normalized by the maximum total intensity of the respective profiles. Green dots with errorbars - polarization position angles (PA,  $\psi = 0.5 \arctan(U/Q)$ ). Magenta dots in  $\chi$  panel with errorbars - ellipticity angle (EA,  $\chi = 0.5 \arcsin(V/\sqrt{Q^2 + U^2 + V^2})$ ). (ii) Intensity profiles at different observation frequencies. 38 MHz: Pilia et al. (2016); 119 MHz: Bilous et al. (2016); 326 MHz: Olszanski et al. (2019); 610 MHz: Gould & Lyne (1998); 1250 MHz: this paper; 1642 MHz: Gould & Lyne (1998); 4850 MHz: Hoensbroech (1999). All higher-frequency profiles are shifted in longitude to be roughly aligned (achieve minimum residual between profiles) with the 38 MHz profile. (iii) A zoomed in version of the left plot with a  $L/I$  panel. Three vertical grey dashed lines represent the longitudes  $-0.925^\circ$ ,  $-0.457^\circ$  and  $0.875^\circ$ . (iv) A zoomed in version of the middle plot. In the  $\psi$  panel, a purple dotted curve and a yellow dotted curve are added, which represents the PA curve shifted by  $45^\circ$  and  $90^\circ$ . Only longitudes where  $L/\sigma_L > 10$  are chosen for plotting ( $\sigma_L$  is the standard deviation of  $L$  in off-pulse longitude range).

The integrated profile of all pulses is shown in Figure 1, where the total intensity ( $I$ ), linear polarization intensity ( $L$ ), circular polarization intensity ( $V$ ), PA ( $\psi$ ) and ellipticity angle (EA,  $\chi$ ) at each longitude are plotted. There is a precursor component on the leading edge of profile, which contributes to the long extension of PA and EA curves to the left. Definitions of PA and EA are in Eq. A12 and A13. The polarization profiles are in accord with the results in Weisberg et al. (1999). B1919+21’s polarization is complex, with a PA curve that vastly deviates from Rotating Vector Model (RVM) curves (Radhakrishnan & Cooke 1969). Except for longitudes around the leading and trailing edges of the pulse profile, the linear polarization fraction ( $L/I$ ) is small ( $< 0.2$ ).

In the longitude range of the leading component, the PA curve shows three “discontinuities”, which are marked with three vertical grey dashed lines in Figure 1. The first one is a nearly  $90^\circ$  jump at longitude  $-0.925^\circ$ , accompanied with a local minimum in  $L$  and  $L/I$ , and a sign change of  $V$  and  $\chi$ . The second one is a  $45^\circ$  ( $135^\circ$ , most clear in Figure 1 (iii)) jump at longitude  $-0.457^\circ$  with a local minimum in  $L$  and  $L/I$ , and a local maximum in  $|V|$  and  $|\chi|$ . The third one is a nearly  $45^\circ$  mild jump at longitude  $0.875^\circ$  with a local minimum in  $L$  and  $L/I$ , and a local maximum in  $|V|$  and  $|\chi|$ . After the third “discontinuity”, the PA curve is continuous but distorted, characteristic with low  $L/I$ , in the central region of the pulse profile. The  $V$  and  $\chi$  curves are also complex. The first “discontinuity” could be interpreted as the change of dominant mode between two orthogonal polarization modes (OPMs), whose existence has

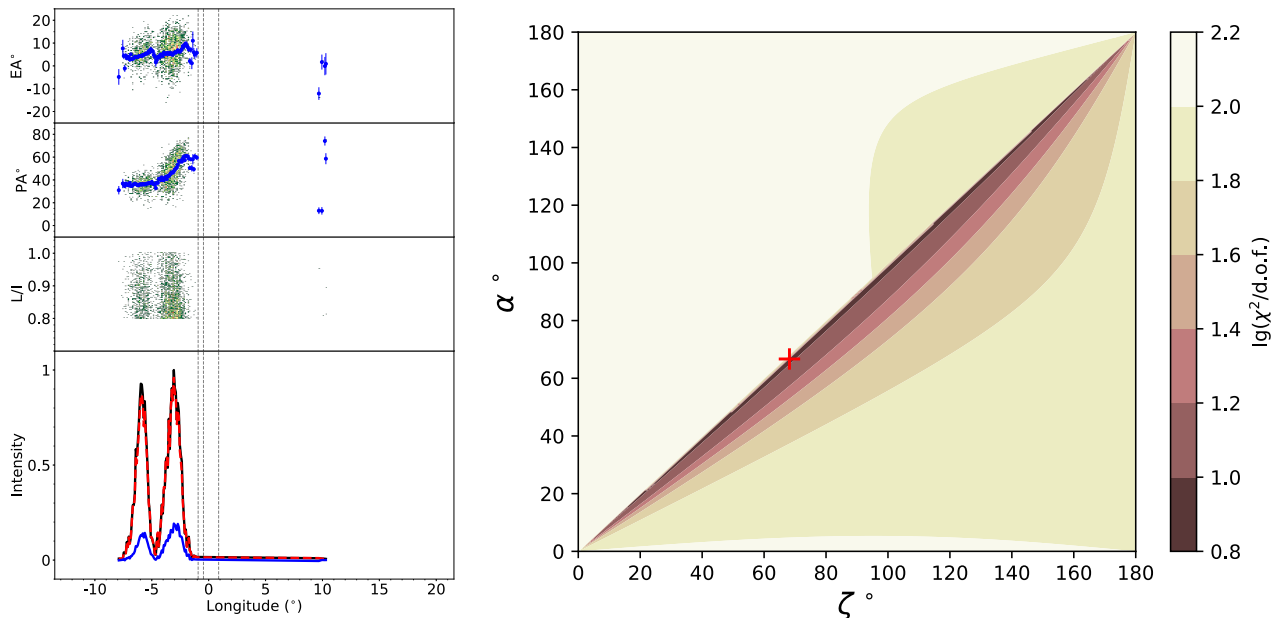


**Figure 2.** Left: profile from adding only highly linearly polarized pulse bins (for details please refer to the text in Section 3.2). The lowest panel: the polarization profile, lines’ meanings are same as Figure 1. The other 3 panels: distributions of  $L/I$ , PA ( $\psi$ ) and EA ( $\chi$ ) versus longitude. The blue dots with errorbars in PA and EA panels are directly calculated (through Eq. A12 and A13) from the highly polarized pulse profile in the lowest panel. Right: the common logarithm values of chi-square (divided by degree of freedom) of fitting RVM curve of given  $(\alpha, \zeta)$  to the modified PA curve. The red “+” sign marks the  $(\alpha, \zeta)$  where we get the smallest  $\chi^2$ .

been reported by former observations (e.g., Mitra et al. 2015). The third one has also been recorded and discussed before (e.g., Mitra et al. 2015; Dyks 2017), which is associated with coherent summation of OPMs. The second one, however, seems newly discovered, and may have an origin similar to the third “discontinuity”.

We’ve also added our intensity profile into a sequence of pulse profiles under different frequencies, shown in Figure 1 (iv). This plot confirms the profiles’ widening when frequency increases. The references for other frequencies’ profiles are provided in the caption.

### 3.2. Attempts at deriving radiative geometry

To derive radiative geometry, we adopt the method that is put forward in Mitra et al. (2023) and tested in Johnston et al. (2024). Practically, at each longitude, we choose all samples having linear polarization fraction  $L/I > 0.8$  and PA measurement error  $\sigma_{PA} < 5^\circ$ , to add them up and form a highly linearly polarized profile. The result is shown in Figure 2. Comparing with the total integrated profile in Figure 1, highly linearly polarized signals only appear at on-pulse window’s edges, and represent only one of the OPMs. We tried RVM curve fitting of the PA dots in the highly linearly polarized profile: for each pair of  $(\alpha, \zeta)$ , we calculate the least chi-square value when changing  $(\psi_0, \phi_0)$  ( $\phi_0$  is limited between  $-90^\circ$  and  $90^\circ$ ). The fitting process is same as that in Cao et al. (2024). The minimum chi-squares plot is also presented in Figure 2. For B1919+21, the inclination angle  $\alpha$  is poorly constrained, but the impact angle  $\beta = \zeta - \alpha$  seems constrained to a small value, which is consistent with the estimation by Kuz’min & Wu (1992) based on the radiation cone model. In all plots, the  $\phi = 0^\circ$  longitude is chosen as the best fitting of  $\phi_0$ , which is near the leading component peak’s longitude.

### 3.3. Single pulses’ polarization distributions

Firstly we calculate the 2D histogram of  $L/I$ , PA and EA for all pulses in the on-pulse window, and the result is shown in Figure 3. In the PA panel, we directly see enhancements of single-pulse PA distributions that represent two

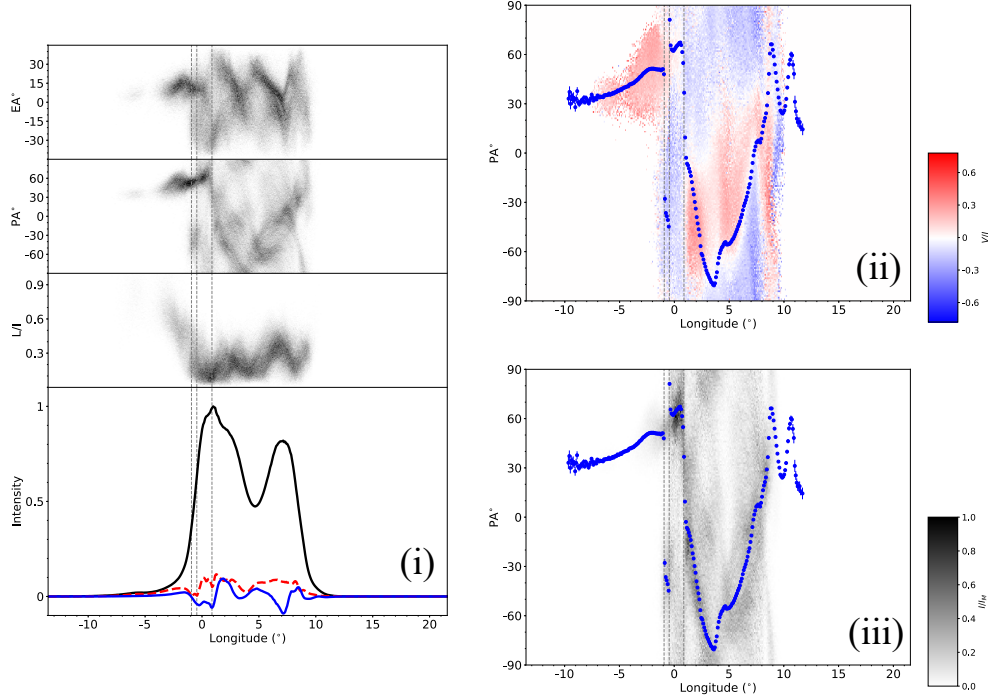


**Figure 3.** (i) Distributions of PA, EA and  $L/I$  versus longitude, of all 2 observation epochs’ 2947 pulses. Panel 4 (1-4 from up to bottom): the integrated profiles of all pulses taken into account, where lines’ meanings are same as Figure 1; Panel 3: the distributions of  $L/I$ ; Panel 2: the distributions of PA. Panel 1: the distributions of EA. For panel 1, 2 and 3, the distribution is more concentrated when color turns darker. In all panels, three vertical grey lines are the same as that of Figure 1. (ii) Distribution of circular polarization fraction painted on  $\phi - \psi$  plot (for calculation details please refer to the text). (iii) Similar plot for intensity distribution (normalized with the maximum intensity value in the distribution). Only single pulses’ bins where both  $\sigma_{PA} \leq 5^\circ$  and  $\sigma_{EA} \leq 5^\circ$  are included, to make sure that all presented points are with significant linear and circular polarization. The blue dots with errorbars are calculated from the integrated profile, same as Figure 1.

OPMs, around the longitude range of the first two vertical grey dashed lines. On the right side of the third dashed line, even the individual pulses’ PA distribution doesn’t seem to follow RVM-like tracks, though OPMs are likely to also appear at longitude  $3 \sim 4^\circ$ . The EA’s distribution forms several tracks, varying from positive values to negative values.

The histograms in Figure 3 (i) are made by counting the number of pulses within the longitude and PA bins. For a given longitude  $\phi$  and a given PA  $\psi$ , we calculate the average circular polarization fraction ( $\bar{V}/\bar{I}$ ) and average intensity  $\bar{I}$  of samples whose longitudes are within  $(\phi, \phi + \Delta\phi)$  and PAs are within  $(\psi, \psi + \Delta\psi)$ . We choose  $\Delta\phi = 360^\circ/4096$ , and  $\Delta\psi = 1^\circ$ . The histograms of the average circular polarization fraction ( $\bar{V}/\bar{I}$ ) and average intensity  $\bar{I}$  are shown in Figure 3 (ii) (iii) respectively. The  $V/I$  distribution plot shows the difference in circular polarization senses for OPMs around  $\phi = -1^\circ$ , which is natural for normal wave modes in magnetized plasmas (e.g., Beskin & Philippov 2012; Cao et al. 2024). Moreover, in the central region ( $1^\circ < \phi < 8^\circ$ ), the  $V/I$  sense distribution is related to the integrated profile’s PA curve: in longitude range ( $1^\circ, 3^\circ$ ), the integrated profile’s PAs correspond to  $V > 0$ ; while in longitude range ( $6^\circ, 8^\circ$ ), the integrated PA curve seems to be located around the  $V = 0$  region in the histogram for individual pulse bins. Such distributions should have some physical implications.

### 3.4. Rapid rotating polarization orientations in single pulses

Next we directly investigate the individual pulses. Several pulses are presented in Figure 4, with polarization evolution tracks on Poincaré spheres plotted alongside. The polarization states of individual pulses still seem irregular, with PA tracks appearing more arbitrary. Not all pulses show “discontinuities” around all three vertical grey dashed lines. Orthogonal mode jumps appear in some pulses’ central longitude ranges (e.g., #274 in Figure 4, at longitude  $\sim 5^\circ$ ). It’s worth noticing that some pulses present monotonically rotating long PA curves in some longitude ranges

(see #7, #275, #555 and #2565 in Figure 4 for example). The PA in those pulses rotates by over  $180^\circ$  or even  $360^\circ$  across longitudes, accompanied with manifest oscillations of circular polarization (or ellipticity angle) values around 0. The polarization states at these pulse longitudes seem to follow long circular tracks on Poincaré spheres.

Such rapid rotating polarization patterns are not rare for B1919+21, with over 1/3 pulses showing quasi-monotonic rapid rotations of PA in some longitude ranges. This phenomenon seems to depend only very weakly on frequency (see Figure 4 for three examples), at least in our observational bandwidth. In addition, considering PA curves as functions of pulse longitudes, most quasi-monotonic PA curves in single pulses have a generally negative slope (e.g., #7, #555 and #2565 in Figure 4), while only very few of them have a positive slope (e.g., #275 in Figure 4). This asymmetry in PA curve slopes' distribution might have some physical implications, which we will discuss later. Finally, we'd like to point out that the PA curves between two adjacent pulses (e.g., #274 and #275 in Figure 4) can change vastly.

#### 4. ATTEMPTS AT MODELING

Among the observed phenomena, the rapid rotating polarization orientations in single pulses are outstanding. The PA curves are far from the RVM types. OPM jumps in integrated profile and single pulses lead us to seek solutions from OPM related mechanisms. Coherent or partially coherent summation of orthogonal polarized waves (e.g., Dyks 2019; Oswald et al. 2023), allowing only varying amplitude ratio, requires that the emitted radio wave's polarization orientation should be initially rotating at different longitudes (to result in over  $360^\circ$  rotation of PA), before propagating. The origin of such a large intrinsic rotation mechanism seems unclear. In this section, we seek solutions based on propagational effects in the magnetosphere. Accompanied by the PA curve, the circular polarization oscillation could indicate the change of phase lags between the wave modes across longitudes, which should be taken into consideration.

##### 4.1. A phenomenological model: phase lag driven

To reproduce the observed polarization variations in single pulses, here we put forward a phenomenological model based on propagational effects. Based on theories like Cheng & Ruderman (1979); Lyubarskii & Petrova (1998); Petrova & Lyubarskii (2000), a pulsar magnetosphere could be divided into the adiabatic walking region (the magnetic field is strong enough and normal modes are linearly polarized) and the polarization limiting region (the weakening or deflection of local magnetic fields introduces more circular polarization components). Here we simply assume that two initially mutually orthogonal radio waves (O wave and E wave) propagate through two plasma layers. Directions of magnetic fields in two layers are fixed separately: in the first layer, the magnetic field is aligned with the O wave electric field vector; in the second layer, the magnetic field has an angle  $\theta_0$  deflected from the first layer's magnetic field. The phase lag between O wave and E wave increases by a value  $\eta$  through propagating in the first layer. In the second layer, the original O and E waves are decomposed into new normal wave modes, between which the phase lag increases by  $\delta$  through propagating. To include depolarization, we also follow Oswald et al. (2023) to introduce coherence  $C$  into our modeling, and then a part of waves are added incoherently. The mathematical details of our model construction are in Appendix A. Schematic diagrams of the model described above are shown in Figure 5 (i).

There are 5 parameters in the model: (1) initial amplitude ratio  $E_O/E_E$ ; (2) first layer's phase lag  $\eta$ ; (3) magnetic field deflection  $\theta_0$ ; (4) second layer's phase lag  $\delta$ ; (5) coherence  $C$ . An example of a pulse simulated from the model is shown in Figure 5 (iii). For this pulse, the parameters are chosen as follows: (1)  $E_O/E_E = 1$ ; (2)  $\eta$  ranges from 0 to  $6\pi$  on each bin, from left to right; (3)  $\theta_0 = 20^\circ$ ; (4)  $\delta = \pi/4$ ; (5)  $C = 0.5$ . Comparing with pulses in real data (e.g. #555 in Figure 5 (iv)), our modeling works well for understanding the polarization variations within individual pulses. The PA curve of the simulated pulse varies by  $3\pi$  across the range monotonically, and the oscillating circular polarization (or EA) is also reproduced. For normal modes in pulsar radiation, when the phase lag between them quickly varies along pulse longitudes, rapid change of polarization pattern could take place in single pulses.

A natural requirement of our model to work is that none of the orthogonal modes should dominate too largely, in other words,  $E_O/E_E$  should be close to 1. Finally, we'd like to emphasize that for explaining the observed polarization rotations, one plasma layer, for which the normal wave modes are elliptical, is equivalent to the two plasma layers described above.

##### 4.2. Calculations on the phase lag between wave modes

We argue that the phase lag between wave modes plays a key role in the physics behind the observed rapid rotating single pulse polarization orientations. Discussions on relations between polarization orientations and phase lags have been made in Jones (2016, 2020), though they intended to avoid too quick changes in polarization. Observed single

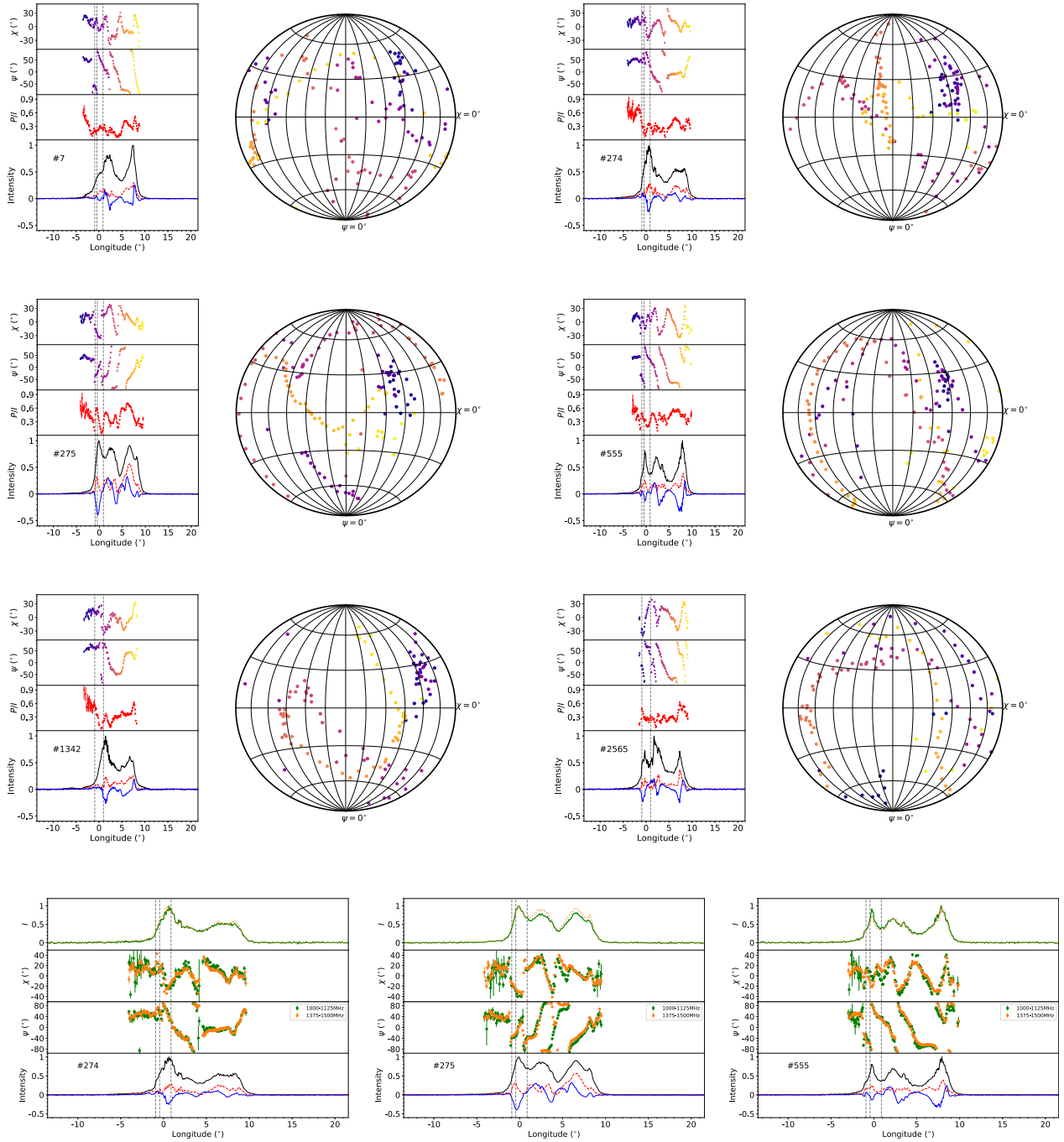


**Figure 4.** (i) Upper 6 plots: 6 single pulses with their polarization states shown on Poincaré spheres. In “Intensity” panels, the lines’ meaning are same as Figure 1. “P/I” panels show the polarization fraction  $\sqrt{Q^2 + U^2 + V^2}/I$  with errorbars on each longitudes (only longitudes where  $\sigma_{PA} \leq 5$  are chosen, same for “ $\psi$ ” panels and “ $\chi$ ” panels). “ $\psi$ ” panels show PAs with errorbars, and “ $\chi$ ” panels show EAs with errorbars, on each chosen longitudes. PA and EA dots are also plotted on Poincaré spheres under Hammer-Aitoff projection. The change of color from darker to lighter of PA and EA dots represents the increase in longitude. (ii) Lower 3 plots: 3 single pulses with PA, EA and total intensity  $I$  plotted in two frequency subbands (1000-1125 MHz in green and 1375-1500 MHz in orange). In the  $I$  panel, the intensity curves are normalized to the maximum values separately for two subbands.

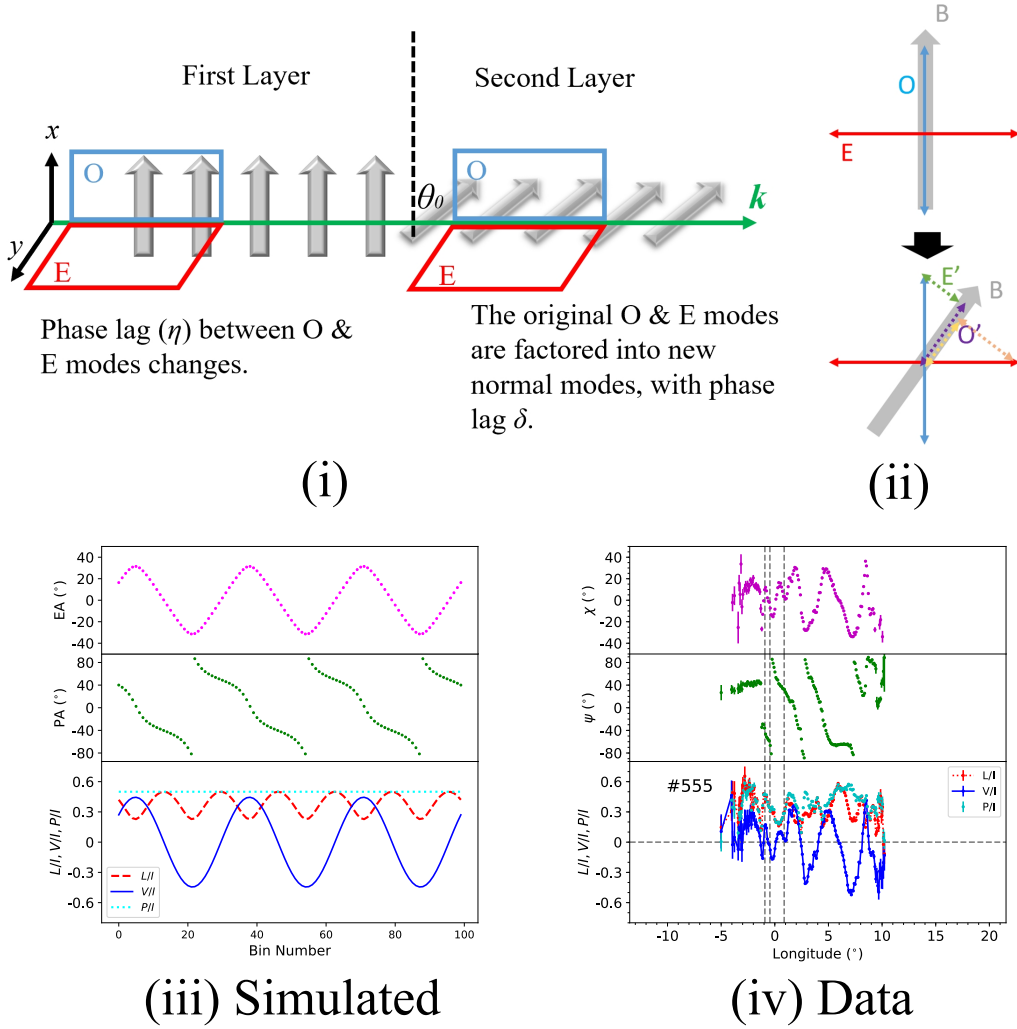


**Figure 5.** (i) A schematic diagram for the phenomenological model. The grey arrows represent magnetic fields. The green long arrow with label “ $k$ ” means the direction of wave propagation, where refraction is neglected. The blue rectangle with label “O” and the red parallelogram with label “E” represent O mode wave and E mode wave. (ii) A cross-sectional view of (i), and also a schematic diagram for the difference between two plasma layers. (iii) A pulse simulated from the phenomenological model. The horizontal axis is the number of sample bins, which is equivalent to the longitude. The red dash line, the blue line and the cyan line are linear, circular and total polarization fraction on each bin. The green and magenta dots are PA and EA on each bin. (iv) linear, circular, total polarization fraction, as well as PA and EA on each bin of pulse #555 in Figure 4.

pulses’ PA can monotonically rotate by values larger than  $\pi$ , which requires the phase lags’ difference, between the end longitude and the start longitude, to be larger than  $2\pi$ , and thus phase lags themselves should be at least of the same order of  $2\pi$ . This requirement may put some constraints on the magnetospheric parameters.

Theoretical estimations of phase lag start from the dispersion relation of normal modes. We adopt the dispersion relation of O and E modes in a relativistic cold plasma with a single bulk velocity and infinitely large magnetic field Melrose & Stoneham (1977); Arons & Barnard (1986), which could be represented as:

$$(1 - n_O^2 \cos^2 \theta) \left[ 1 - \frac{\omega_p^2}{\omega^2 \gamma^3 (1 - n_O \beta \cos \theta)^2} \right] - n_O^2 \sin^2 \theta = 0, \quad n_E = 1 \quad (1)$$

where  $n_O$  and  $n_E$  are refraction indices of O and E modes,  $\theta$  is the angle between wave propagation direction and local magnetic field, and  $\omega_p = \sqrt{e^2 n_e / \epsilon_0 m_e}$  is the plasma (angular) frequency. We consider electron-positron plasma here.



$\gamma = \sqrt{1/(1 - v^2/c^2)} = \sqrt{1/(1 - \beta^2)}$  is the Lorentz factor of magnetospheric particles. Propagation in a trajectory  $L$  leads to a phase lag:

$$\eta = \int_L (k_E - k_O) dl = \int_L \frac{\omega}{c} (n_E - n_O) dl \quad (2)$$

$l$  is related to  $\theta$ , so  $n_O$  is the only variable depending on  $l$  in the integrand in Eq. 2, according to Eq. 1. In a realistic magnetosphere,  $\theta$  changes during propagation because magnetic field's direction is not fixed along the ray trajectory. In other words,  $\theta$  also depends on  $l$ . Considering the fact that observed rapid rotating polarization orientations in single pulses have very weak dependence on frequency,  $n_O$ 's frequency dependence, which is actually affected by  $\theta$  value, is to be investigated below. Numerical solution of Eq. 1 shown in Figure 6 (ii) tells us that the frequency dependence of  $n_O$  (or  $\omega(n_E - n_O)$ ) is weakest at  $\theta = 0^\circ$  and strongest at  $\theta = 90^\circ$ . The case for very small  $\theta$  works better for explaining the weak frequency dependence of rapid polarization rotations we observe.

Given the magnetic field configuration and the distribution of plasma particles, the phase lag between O and E waves of every ray trajectory could be derived. In a dipolar magnetic field,  $\theta$  always becomes larger when waves propagate outward, so a small  $\theta$  in the whole propagational trajectory prefers the emission to originate relatively close to the magnetic axis, which is also in accord with a small  $\beta$  value we've mentioned in Section 3.2. For now, we only consider aligned rotator ( $\alpha = 0^\circ$ ). For oblique rotators, discussions are made in Section 5.1.

Our main assumptions and approximations for the calculation are: (a) pure dipolar magnetic field; (b) ray trajectories are straight lines, where refraction is neglected; (c) wave propagation direction follows only the tangential direction of magnetic field at the emission point; (d) the plasma particle number density decreases as the distance to pulsar center  $r$  increases, in the form (similar to Eq. (51) in Ruderman & Sutherland (1975)):

$$n_e(r) = \kappa \cdot n_{\text{GJ,surf}} \cdot \left(\frac{R_{\text{NS}}}{r}\right)^3 = \kappa \cdot 7 \times 10^{10} \left(\frac{B_{\text{surf}}}{10^{12}\text{G}}\right) \left(\frac{P}{1\text{s}}\right)^{-1} \cdot \left(\frac{R_{\text{NS}}}{r}\right)^3 \text{ cm}^{-3} \quad (3)$$

where  $n_{\text{GJ,surf}}$  is the Goldreich-Julian number density at pulsar surface (Eq. (9) in Goldreich & Julian (1969)),  $B_{\text{surf}}$  is the surface magnetic field strength estimated with period  $P$  and period derivative  $\dot{P}$  (see Philippov & Kramer 2022 for example). The neutron star radius  $R_{\text{NS}}$  is assumed simply to be 10km.

Integration of equation (2) begins at the emission point and ends at the light cylinder. Given  $l$ ,  $n_O$  is determined through calculating  $\theta$ —then the whole integrand is determined. A schematic diagram of the integration path is shown in Figure 6 (i). With  $\kappa = 100$ ,  $\gamma = 1000$ , the calculated phase lags on different frequencies are plotted in Figure 6 (iii). Under these parameter values,  $\eta$ s lie in the same orders of  $2\pi \sim 6\pi$ . A larger  $\kappa$  or a smaller  $\gamma$  lead the phase lag to be larger. When emission height is lower, the phase lag is also larger, and the frequency dependence is weaker. The absence of spectral evolution of observed polarization rotation suggests a small emission height for B1919+21.

## 5. DISCUSSION

### 5.1. Comments on modeling in Section 4

Some of our choices of parameters in Section 4.1 are mainly for simplicity. We let  $\eta$  vary but  $\delta$  keep constant—this assumption could be adjusted to let both  $\eta$  and  $\delta$  change, which could happen in real magnetospheres because of the difference on plasma particle distribution, for example. In addition,  $E_O/E_E$ ,  $\theta_0$  and  $C$  need not to be constant along pulse longitudes. Our phenomenological model could be applied to explain other polarization behaviours in pulsars, but we do not go into detail here.

Eq. 1 is based on the assumption that the magnetic field is large enough. Quantitatively, validation of Eq. 1 requires  $\omega_B \gg \omega$ , where  $\omega_B = eB/m_e c$ . With dipole field  $B \approx 10^{12}(R_{\text{NS}}/r)^3\text{G}$  we have  $\omega_B = 1.8 \times 10^{19}(R_{\text{NS}}/r)^3\text{s}^{-1}$ . So Eq. 1 is valid at least within  $10^3 R_{\text{NS}}$  from the neutron star centroid. And because plasma particle number density decreases quickly when  $r$  increases (Eq. 3), the integration of Eq. 2 will hardly differ between integrating to light cylinder and integrating to  $\sim 10^3 R_{\text{NS}}$ . The inner magnetosphere contributes to the phase lag most—this is also valid for oblique rotators ( $\alpha > 0$ ).

$\eta$  in Section 4.2 is evaluated to be on the order of  $2\pi$ . To achieve rapid polarization rotations in single pulses,  $\eta$  might be larger, which demands corresponding  $\kappa$  to be larger or  $\gamma$  to be smaller. But the requirement of low emission height should always be satisfied.

### 5.2. Bifurcated emission component in highly linearly polarized profile

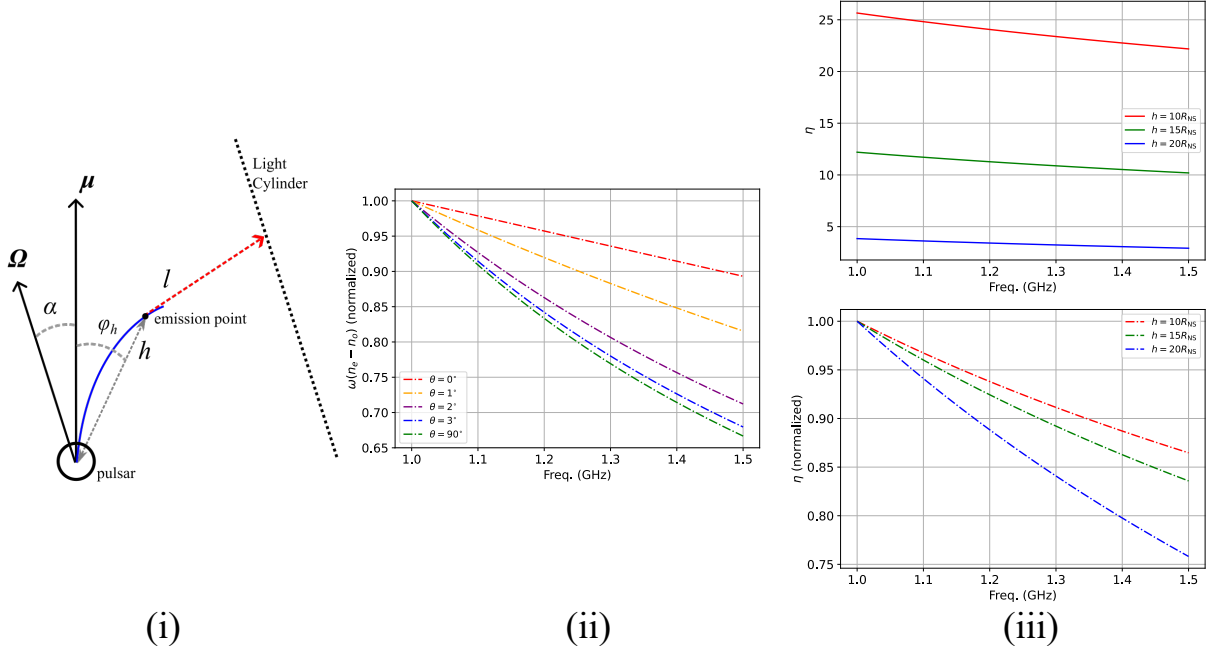


**Figure 6.** (i) A schematic diagram of the phase lag calculation. (ii) Results of numerically solving Eq. 1, presented in  $\omega \cdot (n_E - n_O)$ 's dependence on frequency, given different  $\theta$ . For each curve, the values are normalized with the maximum of the curve, namely the  $\omega \cdot (n_E - n_O)$  value at 1 GHz.  $\gamma$  is chosen 100, and  $n_e = 10^9 \text{cm}^{-3}$ . (iii) Phase lags (original values and normalized values) between O and E modes versus frequency, with parameters  $\kappa = 10^2$ ,  $\gamma = 10^3$ ,  $\alpha = 0^\circ$  and  $\phi_h = 1^\circ$ . Red, green and blue lines represent results calculated with  $h = 10, 15$  and  $20$  times of  $R_{NS}$ . For details of the theoretical constructions please refer to the text in Section 4.2.

In Figure 2, the highly linearly polarized profile has two emission components at the leading edge of the total integrated profile. The two components are close to each other, with a large depth in between. Such phenomenon is similar to the bifurcated emission component studied in Dyks et al. (2010); Dyks (2023). In some pulsars' integrated profiles, bifurcated emission components are attributed to a curvature-radiation-induced split fan beam, where only the ordinary mode component is Doppler shifted into the observed bandwidth through the scattering (Dyks 2023). We observe only one patch of OPM in Figure 2's bifurcated component, which is also consistent with the model. The bifurcated component is invisible in the total integrated profile (Figure 2 (i)), where only a small precursor component is seen.

### 5.3. On asymmetries in B1919+21's polarization patterns

We'd like to emphasize two asymmetries in our observational facts. One is that from the RVM fitting, the centroid of the PA curve seems to arrive manifestly earlier than the centroid (valley) of the integrated pulse's profile of total intensity, which contradicts the model of relativistic aberration (BCW model, Blaskiewicz et al. 1991), assuming a symmetrically filled beam. The other, which is more rigid, is that most monotonic long PA curves (cover  $> 180^\circ$ ) in single pulses have a negative slope, while only very few of them have a positive slope. Both asymmetries could be interpreted as consequences of the asymmetric distribution of magnetospheric plasma particles' number density or Lorentz factor, or of discharge positions near the pulsar surface. In the case of our theoretical explanation, PA slopes imply the increase or decrease of phase lag between O and E modes versus longitude, which depends on distributions mentioned above.

Considering the fact that PA curves could change greatly between adjacent pulses (see #274 and #275 in Figure 4 for examples), and that the dispersion relation (Eq. 1) depends sensitively on Lorentz factor  $\gamma$ , single pulses' polarization pattern may mostly be affected by the  $\gamma$  distribution of plasma particles in the magnetosphere. Distributions of particle number density and discharge positions seem more likely to be almost fixed, although they may be asymmetrical about the fiducial plane (where line of sight, magnetic axis and rotational axis are coplanar), probably due to some particular surface structures (e.g., Xu 2024; Wang et al. 2024).

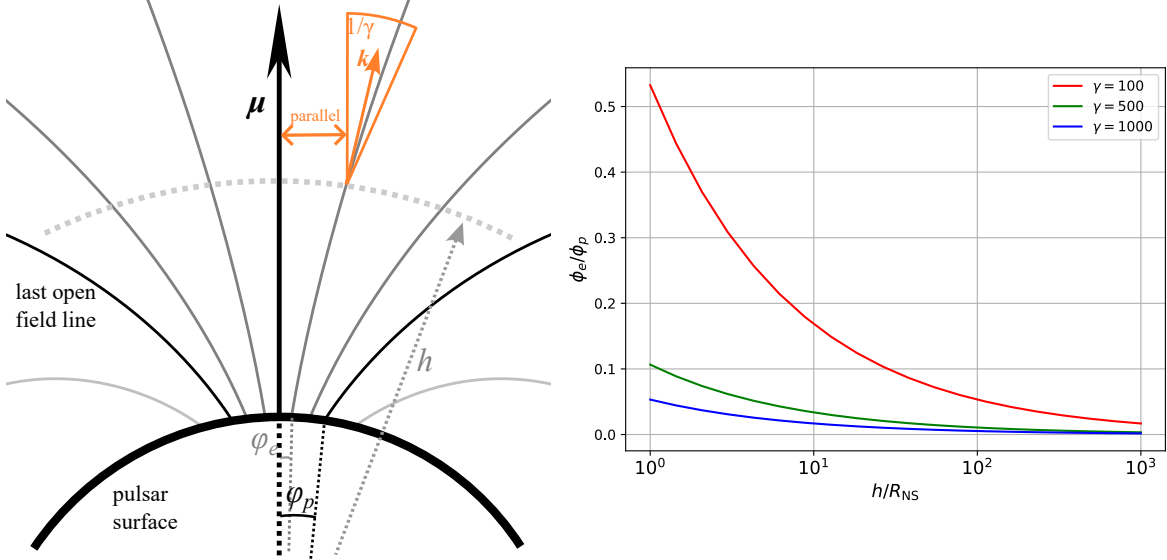


**Figure 7.** Left: Schematic diagram for emission region above a pulsar’s polar cap. The grey and thin black curves represent dipolar magnetic field lines. The thick circular arc means the pulsar surface. The orange sector means the radiation cone of  $1/\gamma$ . The orange arrow with label “ $\mathbf{k}$ ” is the wave emission/propagation direction, which is tangential to local magnetic field. For other details, please refer to the text. Right:  $\phi_e/\phi_p$ ’s dependence on  $h/R_{\text{NS}}$ , plotted with 3 different values of  $\gamma$  (100, 500 and 1000, marked with red, green and blue colors).

#### 5.4. Why B1919+21 is “special”?

Although we have not achieved good RVM fitting in this paper, low emission height required in Section 4.2 seems to also support the alignment of magnetic axis and line-of-sight, which may also account for B1919+21’s relatively high brightness. The coherence of orthogonal wave modes, which could be related to the question where orthogonal modes are generated, needs further considerations.

The low  $L/I$  in both B1919+21’s integrated profiles and single pulses also indicate significant incoherent superposition of waves. Such superposition may be related to the low emission height. To clarify the relation between emission height and wave superposition, we draw a schematic diagram of the radiative region above pulsar surface, in Figure 7 (left). We could receive radio waves from different emission points, where the radiation is concentrated within a  $1/\gamma$  cone due to relativistic beaming. In the following discussion, we assume constant emission height  $h$  and radiating particles’ Lorentz factor  $\gamma$ . When our line-of-sight is fixed, for example parallel to the magnetic axis, the emission points visible to us are determined by the positions and orientations of  $1/\gamma$  cones. We mark the angle between line-of-sight and foot of magnetic field line, where the  $1/\gamma$  cone’s inner edge is parallel to the line-of-sight, as  $\phi_e$ . The ratio of  $\phi_e$  to the angular radius of polar cap  $\phi_p$  can describe the degree of overlapping between different  $1/\gamma$  cones. Figure 7 (right) shows  $\phi_e/\phi_p$ ’s dependence on  $h$  and  $\gamma$ . Smaller  $h$  leads to larger  $\phi_e/\phi_p$ , which indicates more significant incoherent mixing of waves from different  $1/\gamma$  cones.

However, B1919+21 may not be “special” for its rapid rotating polarization orientations in single pulses, because many pulsars actually lack detailed single pulse investigations of polarization. A more refined model might be achieved after more similar or relevant phenomena are analyzed.

## 6. CONCLUSION

The FAST observational results of PSR B1919+21 are presented in this manuscript. The integrated profile’s complex PA curve and circular polarization variation result from the rapid rotating polarization orientations in single pulses. In many observed single pulses, the PA could monotonically rotate over  $180^\circ$  or even  $360^\circ$  across longitudes, and is always accompanied with circular polarization variations that could change handedness. Most of those quasi monotonic PA curves have negative slopes.

We attribute the phenomena to the difference in normal modes’ phase lags between different pulse longitudes, and build a simple model based on propagational effects that can reproduce the observed polarization patterns in single

pulses. An appropriate value of phase lag between O and E waves requires appropriate values of pulsar magnetosphere's multiplicity  $\kappa$  and secondary plasma's Lorentz factor  $\gamma$ . The emission height should be low enough to fit the weak frequency dependence of the polarization rotations. We argue that the distribution of plasma number density, of discharge points near pulsar surface, or of secondary particles' Lorentz factor  $\gamma$ , should be asymmetric around the fiducial plane to explain the asymmetry observed in single pulses' monotonic PA curves' slopes.

Still we are not sure if B1919+21 is "special" for exhibiting such single pulse polarization pattern. Except for the requirement of more single pulse investigation of this pulsar under other frequency bands, we appeal that researchers do more single pulses studies on more known pulsars, for a better understanding of radio pulsars' radiation and magnetospheres.

SSC wants to thank Prof. Gregory Herczeg at KIAA, Peking University. Through his "Advanced Writing for Astronomy" course, SSC's writing of this paper had been improved. Shenglan Sun at Peking University also gave useful comments on the paper during the writing course by Gregory. JD acknowledges funding by the National Science Centre, Poland, grant no. 2023/49/B/ST9/01783. All data used in this work is from the Five-hundred-meter Aperture Spherical radio Telescope (FAST). FAST is a Chinese national mega-science facility, operated by National Astronomical Observatories, Chinese Academy of Sciences. This work is supported by the National SKA Program of China (2020SKA0120100), the National Natural Science Foundation of China (Nos. 12003047 and 12133003), and the Strategic Priority Research Program of the Chinese Academy of Sciences (No. XDB0550300). Part of this research (Figure 1's (ii)) has made use of the EPN Database of Pulsar Profiles maintained by the University of Manchester, available at: <http://www.jodrellbank.manchester.ac.uk/research/pulsar/Resources/epn/>.

## APPENDIX

### A. FORMULA FOR CONSTRUCTING THE PHENOMENOLOGICAL MODEL

The mathematical details of the model described in Section 4.1 are presented in this section. We mark the initial O and E waves' electric field vector amplitudes as  $E_O$  and  $E_E$ .  $E_{O,0}^{(C)} = C \cdot E_O$  and  $E_{E,0}^{(C)} = C \cdot E_E$  represent the coherently added part, while  $E_{O,0}^{(I1)} = (1 - C) \cdot E_O$ ,  $E_{E,0}^{(I1)} = 0$  and  $E_{O,0}^{(I2)} = 0$ ,  $E_{E,0}^{(I2)} = (1 - C) \cdot E_E$  represent the incoherently added part (same as the settings in Oswald et al. 2023). After propagation in the first plasma layer, the electric field vectors become:

$$E_{O,1}^{(C;I)} = E_{O,0}^{(C;I)} \quad (\text{A1})$$

$$E_{E,1}^{(C;I)} = E_{E,0}^{(C;I)} e^{i\eta} \quad (\text{A2})$$

and after propagating through the second plasma layer, the electric field vectors become:

$$E_{O,2}^{(C;I)} = E_{O,1}^{(C;I)} \cos \theta_0 + E_{E,1}^{(C;I)} \sin \theta_0 \quad (\text{A3})$$

$$E_{E,2}^{(C;I)} = (-E_{O,1}^{(C;I)} \sin \theta_0 + E_{E,1}^{(C;I)} \cos \theta_0) e^{i\delta} \quad (\text{A4})$$

Then we return to the original coordinates, where the electric field vectors in the original O and E wave directions ( $x$  and  $y$  in Figure 5) are:

$$E_x^{(C;I)} = E_{O,2}^{(C;I)} \cos \theta_0 - E_{E,2}^{(C;I)} \sin \theta_0 \quad (\text{A5})$$

$$E_y^{(C;I)} = E_{O,2}^{(C;I)} \sin \theta_0 + E_{E,2}^{(C;I)} \cos \theta_0 \quad (\text{A6})$$

Finally we can calculate Stokes parameters (e.g., Jackson 1998):

$$I^{(C;I)} = E_x^{(C;I)} (E_x^{(C;I)})^* + E_y^{(C;I)} (E_y^{(C;I)})^* \quad (\text{A7})$$

$$Q^{(C;I)} = E_x^{(C;I)} (E_x^{(C;I)})^* - E_y^{(C;I)} (E_y^{(C;I)})^* \quad (\text{A8})$$

$$U^{(C;I)} = 2\text{Re}[(E_x^{(C;I)})^* E_y^{(C;I)}] \quad (\text{A9})$$

$$V^{(C;I)} = 2\text{Im}[(E_x^{(C;I)})^* E_y^{(C;I)}] \quad (\text{A10})$$

The total Stokes parameters are:

$$S = S^{(C)} + S^{(I1)} + S^{(I2)} \quad (\text{A11})$$

where  $S = (I, Q, U, V)$ . With Stokes parameters we can calculate PA and EA:

$$\text{PA} = 0.5 \arctan(U/Q) \quad (\text{A12})$$

$$\text{EA} = 0.5 \arcsin(V/\sqrt{Q^2 + U^2 + V^2}) \quad (\text{A13})$$

and draw the simulated pulse in Figure 5.

## REFERENCES

- Arons, J., & Barnard, J. J. 1986, *ApJ*, 302, 120  
 Barnard, J. J., & Arons, J. 1986, *ApJ*, 302, 138  
 Beskin, V. S., & Philippov, A. A. 2012, *MNRAS*, 425, 814  
 Bilous, A. V., Kondratiev, V. I., Kramer, M., et al. 2016, *A&A*, 591, A134  
 Blaskiewicz, M., Cordes, J. M., & Wasserman, I. 1991, *ApJ*, 370, 643  
 Cao, S., Jiang, J., Dyks, J., et al. 2024, *ApJ*, 973, 56  
 Cheng, A. F., & Ruderman, M. A. 1979, *ApJ*, 229, 348  
 Cordes, J. M. 1975, *ApJ*, 195, 193  
 Dyks, J. 2017, *MNRAS*, 472, 4598  
 —. 2019, *MNRAS*, 488, 2018  
 —. 2023, *MNRAS*, 522, 1480  
 Dyks, J., Rudak, B., & Demorest, P. 2010, *MNRAS*, 401, 1781  
 Goldreich, P., & Julian, W. H. 1969, *ApJ*, 157, 869  
 Gould, D. M., & Lyne, A. G. 1998, *MNRAS*, 301, 235  
 Hassall, T. E., Stappers, B. W., Hessels, J. W. T., et al. 2012, *A&A*, 543, A66  
 Hewish, A., Bell, S. J., Pilkington, J. D. H., Scott, P. F., & Collins, R. A. 1968, *Nature*, 217, 709  
 Hobbs, G. B., Edwards, R. T., & Manchester, R. N. 2006, *MNRAS*, 369, 655  
 Hoensbroech, A. G. 1999, PhD thesis, -  
 Hotan, A. W., van Straten, W., & Manchester, R. N. 2004, *PASA*, 21, 302  
 Jackson, J. D. 1998, *Classical Electrodynamics*, 3rd Edition (Wiley-VCH)  
 Jiang, P., Tang, N.-Y., Hou, L.-G., et al. 2020, *Research in Astronomy and Astrophysics*, 20, 064  
 Johnston, S., Mitra, D., Keith, M. J., Oswald, L. S., & Karastergiou, A. 2024, *MNRAS*, 530, 4839  
 Jones, P. B. 2016, *MNRAS*, 455, 3814  
 —. 2020, *MNRAS*, 498, 5003  
 Kuz'min, A. D., & Wu, X. 1992, *Ap&SS*, 190, 209  
 Lower, M. E., Kramer, M., Johnston, S., et al. 2024, *MNRAS*, 534, 3936  
 Lyubarskii, Y. E., & Petrova, S. A. 1998, *Ap&SS*, 262, 379  
 Lyutikov, M., & Thompson, C. 2005, *ApJ*, 634, 1223  
 Manchester, R. N., Hobbs, G. B., Teoh, A., & Hobbs, M. 2005, *AJ*, 129, 1993  
 Manchester, R. N., Taylor, J. H., & Huguenin, G. R. 1975, *ApJ*, 196, 83  
 Melrose, D. B., & Stoneham, R. J. 1977, *PASA*, 3, 120  
 Mitra, D., Arjunwadkar, M., & Rankin, J. M. 2015, *ApJ*, 806, 236  
 Mitra, D., Melikidze, G. I., & Basu, R. 2023, *MNRAS*, 521, L34  
 Mitra, D., & Rankin, J. M. 2002, *ApJ*, 577, 322  
 Noordhuis, D., Prabhu, A., Witte, S. J., et al. 2023, *PhRvL*, 131, 111004  
 Olszanski, T. E. E., Mitra, D., & Rankin, J. M. 2019, *MNRAS*, 489, 1543  
 Oswald, L. S., Karastergiou, A., & Johnston, S. 2023, *MNRAS*, 525, 840  
 Petrova, S. A., & Lyubarskii, Y. E. 2000, *A&A*, 355, 1168  
 Philippov, A., & Kramer, M. 2022, *ARA&A*, 60, 495  
 Pilia, M., Hessels, J. W. T., Stappers, B. W., et al. 2016, *A&A*, 586, A92  
 Primak, N., Tiburzi, C., van Straten, W., Dyks, J., & Gulyaev, S. 2022, *A&A*, 657, A34  
 Proszynski, M., & Wolszczan, A. 1986, *ApJ*, 307, 540  
 Radhakrishnan, V., & Cooke, D. J. 1969, *Astrophys. Lett.*, 3, 225  
 Ruderman, M. A., & Sutherland, P. G. 1975, *ApJ*, 196, 51  
 van Straten, W., & Bailes, M. 2011, *PASA*, 28, 1  
 van Straten, W., Manchester, R. N., Johnston, S., & Reynolds, J. E. 2010, *PASA*, 27, 104  
 Wang, Z., Lu, J., Jiang, J., et al. 2024, *Astronomische Nachrichten*, 345, e20240010  
 Weisberg, J. M., Cordes, J. M., Lundgren, S. C., et al. 1999, *ApJS*, 121, 171

Xu, R. 2024, Nuclear Physics Review, 41, 863.  
[http://www.npr.ac.cn/en/article/doi/10.11804/  
NuclPhysRev.41.QCS2023.19](http://www.npr.ac.cn/en/article/doi/10.11804/NuclPhysRev.41.QCS2023.19)

Xue, Z. H., Lee, K. J., Gao, X. D., & Xu, R. X. 2023,  
PhRvD, 108, 083009